Journal of Hydrology 523 (2015) 680–692

Contents lists available at ScienceDirect

Journal of Hydrology

journal homepage: www.elsevier.com/locate/jhydrol

Urban flood modeling with porous shallow-water equations: A case study of model errors in the presence of anisotropic porosity

Byunghyun Kim [a], Brett F. Sanders [a,*], James S. Famiglietti [b,c], Vincent Guinot [d]

[a] Department of Civil and Environmental Engineering, University of California, Irvine, CA 92697, USA
[b] Department of Earth System Science, University of California, Irvine, CA 92697, USA
[c] NASA Jet Propulsion Laboratory, California Institute of Technology, Pasadena, CA 91109, USA
[d] Université Montpellier 2, HydroSciences Montpellier, CC MSE, Place Eugéne Bataillon, 34095 Montpellier Cedex 5, France

ARTICLE INFO

Article history:
Received 24 May 2014
Received in revised form 20 December 2014
Accepted 23 January 2015
Available online 11 February 2015
This manuscript was handled by Konstantine P. Georgakakos, Editor-n-Chief, with the assistance of Ioannis K Tsanis, Associate Editor

Keywords:
Porous shallow water equations
Finite volume model
Anisotropic porosity
Dam-break flood
Urban flood

ABSTRACT

Porous shallow-water models (porosity models) simulate urban flood flows orders of magnitude faster than classical shallow-water models due to a relatively coarse grid and large time step, enabling flood hazard mapping over far greater spatial extents than is possible with classical shallow-water models. Here the errors of both isotropic and anisotropic porosity models are examined in the presence of anisotropic porosity, i.e., unevenly spaced obstacles in the cross-flow and along-flow directions, which is common in practical applications. We show that porosity models are affected by three types of errors: (a) structural model error associated with limitations of the shallow-water equations, (b) scale errors associated with use of a relatively coarse grid, and (c) porosity model errors associated with the formulation of the porosity equations to account for sub-grid scale obstructions. Results from a unique laboratory test case with strong anisotropy indicate that porosity model errors are smaller than structural model errors, and that porosity model errors in both depth and velocity are substantially smaller for anisotropic versus isotropic porosity models. Test case results also show that the anisotropic porosity model is equally accurate as classical shallow-water models when compared directly to gage measurements, while the isotropic model is less accurate. Further, results show the anisotropic porosity model resolves flow variability at smaller spatial scales than the isotropic model because the latter is restricted by the assumption of a Representative Elemental Volume (REV) which is considerably larger than the size of obstructions. These results point to anisotropic porosity models as being well-suited to whole-city urban flood prediction, but also reveal that point-scale flow attributes relevant to flood risk such as localized wakes and wave reflections from flow obstructions may not be resolved.

1. Introduction

Urban flood modeling is now possible at centimetric resolution or better with modern laser scanning data and flood models (Bates, 2012; Sampson et al., 2012), but it is not advisable at this resolution over entire floodplains as the computational costs and memory demands are forbidding except on massively parallel computing architectures. Commonly used models are constrained by the Courant, Friedrichs, Lewy (CFL) condition for both stability and accuracy which dictates nearly an order-of-magnitude increase in computational effort every time the mesh resolution is doubled. For a Cartesian grid with a cell size of Δx, the computational cost C of integrating a flood over a specified duration will scale as the product of the required number of computational cells n_c and time steps n_t,

$$C \sim n_c n_t \sim \frac{1}{\Delta x^3} \tag{1}$$

because $n_c \sim \Delta x^{-2}$ and the CFL requirement to scale Δt with Δx. Thus, halving the cell size causes an eight fold increase in computational effort (nearly an order of magnitude) and at least a fourfold increase in memory demands.

Porous shallow-water equations (porosity models) resolve urban flooding at a relatively coarse (and efficient) resolution compared to available geospatial data using additional parameters that account for sub-grid scale topographic features affecting the movement and storage flood water (Defina, 2000; Yu and Lane, 2005; McMillan and Brasington, 2007; Sanders et al., 2008; Soares-Frazão et al., 2008; Cea and Vázquez-Cendón, 2010; Chen et al., 2012; Guinot, 2012; Schubert and Sanders, 2012). In practice, the

* Corresponding author. Tel.: +1 949 824 4327; fax: +1 949 824 3672.
E-mail address: bsanders@uci.edu (B.F. Sanders).
URL: http://sanders.eng.uci.edu (B.F. Sanders).

http://dx.doi.org/10.1016/j.jhydrol.2015.01.059
0022-1694/

idea is to use a cell size on the order of meters or dekameters. This gives rise to models that resolve flooding at the *pore scale* roughly corresponding to the width of roadways and open spaces between buildings, in contrast with classical shallow-water models that resolve flooding at the *point scale*, as approximated by the grid resolution. Importantly, porosity models enable massive reductions in computational effort compared with classical shallow-water models as a result of the scale difference.

Sanders et al. (2008) and Guinot (2012) introduce two alternative formulations of porosity models to capture porosity anisotropy, which can be expected in practical applications. Anisotropy occurs in urban landscapes when there are preferential flow directions such as wide streets and narrow alleys aligned in perpendicular directions. Hypothetical examples of anisotropic flow have been presented in previous studies (Sanders et al., 2008; Guinot, 2012), including numerous cases with angled channel-like flows through urban areas. Additionally, Schubert and Sanders (2012) present a field-scale application of an anisotropic porosity model that outperforms models based on the classical shallow-water equations.

Porosity heterogeneity exists when the size of flow paths is spatially variable, and different porosity models resolve heterogeneity over different scales. Isotropic porosity models are restricted to scales larger than the length scale of the Representative Elemental Volume (REV). This is typically an order of magnitude larger than the scale of flow obstructions in urban flood applications, nominally a kilometer or more (Guinot, 2012). On the other hand, the anisotropic porosity model developed by Sanders et al. (2008) does not require the existence of an REV and can resolve heterogeneity at the grid scale.

Since porosity anisotropy is a critical consideration for practical applications, this study presents modeling of a unique experimental test case involving dam-break flow through an anisotropic array of obstructions, which builds on earlier experimental work and modeling studies focused on isotropic arrays of obstructions (Testa et al., 2007; Soares-Frazão and Zech, 2008). A classical shallow-water model and both isotropic and anisotropic porosity models are applied and calibrated. The objective is to measure and report the magnitude of porosity model errors in an absolute sense and also relative to other errors which collectively limit the overall accuracy of the model. A better understanding of errors is needed to effectively use porosity models in flood hazard mapping. Three types of errors are reported: (a) structural model errors associated with the shallow-water equations which constitute the foundation of the porosity models, (b) scale errors arising from a grid size that matches the pore scale instead of the point scale, and (c) porosity model errors associated the parameterization of sub-grid scale obstructions. Results point to significant differences in porosity model errors between porosity model formulations.

2. Methods and materials

2.1. Porosity definition

Porosity can be defined in more than one way, namely as a volume average fraction of pore space in a porous media or as an areal average fraction of pore space, as in a slice through the porous medium (Bear, 1988). Both volumetric and areal porosity can be expected to vary spatially in the case of a heterogeneous porous medium, and areal porosity can also vary with the orientation of the plane over which the areal average is taken, and thus exhibit anisotropy. If an urban land surface filled with solid features is taken as a porous medium, then the pore space represents the gaps between the solid features, the volumetric porosity represents the fraction of the land surface able to store water, and the areal porosity represents the fraction of space available for flood conveyance which is directionally dependent.

2.2. Porous shallow-water equations

The anisotropic porosity model of Sanders et al. (2008) is written as integral statements of mass and momentum conservation for an arbitrary 2D domain Ω with boundary Γ and unit outward normal vector $\mathbf{n}$ as follows,

$$\frac{\partial}{\partial t}\int_{\Omega} i\mathbf{U}\,d\Omega + \oint_{\Gamma} i\mathbf{E}\cdot\mathbf{n}\,d\Gamma = \oint_{\Gamma} i\mathbf{H}\cdot\mathbf{n}\,d\Gamma + \int_{\Omega} i\mathbf{S}\,d\Omega \tag{2}$$

where

$$\mathbf{U} = \begin{pmatrix} h \\ uh \\ vh \end{pmatrix} \quad \mathbf{E} = \begin{pmatrix} uh & vh \\ u^2h + \frac{1}{2}gh^2 & uvh \\ uvh & v^2h + \frac{1}{2}gh^2 \end{pmatrix} \tag{3}$$

$$\mathbf{S} = \begin{pmatrix} 0 \\ -(c_D^f + c_D^b)uV \\ -(c_D^f + c_D^b)vV \end{pmatrix} \quad \mathbf{H} = \begin{pmatrix} 0 & 0 \\ \frac{1}{2}gh|_{\eta_o}^2 & 0 \\ 0 & \frac{1}{2}gh|_{\eta_o}^2 \end{pmatrix} \tag{4}$$

where u = x-component of velocity, v = y-component of velocity, g = gravitational constant, $V = (u^2 + v^2)^{1/2}$, c_D^f is a ground friction drag coefficient, c_D^b is a drag coefficient for sub-grid scale flow obstructions, and $h|_{\eta_o}$ is the depth corresponding to a piecewise constant water surface elevation η_o and piecewise linear ground elevation z within Ω. The $\mathbf{H}$ term is introduced to transform the classical ground slope source term to a boundary integral that preserves stationary solutions. Based on the limits of this transformation, the momentum equations appearing in Eq. (2) are restricted to numerical schemes that are first- or second order accurate in space (Sanders et al., 2008).

The variable $i(x,y)$ appearing in Eq. (2) is defined for the spatial domain $D \in \mathbf{R}^2$ and represents a binary density function that takes on a value of zero or unity depending on the presence or absence of a solid flow barrier as follows (Sanders et al., 2008),

$$i(x,y) = \begin{cases} 0 & \text{if} \quad (x,y) \in D_b \\ 1 & \text{otherwise} \end{cases} \tag{5}$$

where D_b is a subdomain of D that corresponds to solid obstacles. Two grid-based porosity parameters are dependent on the density function (Eq. (5)) as follows,

$$\phi_j = \frac{1}{\Omega_j}\int_{\Omega_j} i\,d\Omega \qquad \psi_k = \frac{1}{\Gamma_k}\int_{\Gamma_k} i\,d\Gamma \tag{6}$$

where Ω_j corresponds to the two-dimensional (2D) spatial domain of the jth computational cell and Γ_k corresponds to the kth computational edge of a mesh. Note that ϕ_j represents the fraction of a cell area occupied by voids, and ψ_k represents the fraction of a cell edge occupied by voids. Consequently, these parameters affect the relative storage of cells and conveyance between cells, respectively. Importantly, anisotropic blockage effects are explicitly resolved by the distribution of ψ_k values across the computational mesh. It is noted that isotropic porous shallow-water equations can be recovered from Eq. (2) under the assumption that $\phi_j = \psi_k \forall k$. Additionally, Eq. (2) reverts to the classical shallow-water equations in the limit that $i(x,y) = 1$.

Presently it is not clear how well isotropic and anisotropic porosity models resolve flow at the pore scale where information is needed to assess the risks facing individual land parcels in an urban area, especially when the obstructions exhibit anisotropy. Eq. (2) resolves flow properties on a grid-cell by grid-cell basis which corresponds to the pore scale since the model requires a grid

that aligns cells with pore spaces (Sanders et al., 2008). In contrast, isotropic models require the existence of an REV where the porosity is scale-independent and where areal and volumetric porosities converge to a single scalar value (Bear, 1988). The length scale of the REV is roughly an order of magnitude larger than the length scale of obstructions in urban landscapes (Guinot, 2012), so assuming that pore sizes and obstructions are similarly sized, the isotropic models theoretically resolve flow at roughly an order of magnitude larger scale than the anisotropic model presented here. On the other hand, Guinot (2012) suggests that isotropic porosity becomes representative of the converged REV value at scales 2–3 times smaller than the REV scale.

The ground friction drag coefficient is parameterized by a Darcy–Weisbach f as follows, $c_D^f = f/8$ which is in turn computed using a modified form of the Haaland equation (Haaland, 1983) presented by Arega and Sanders (2004) which considers the Nikuradse sand-grain roughness height k_s and the depth-based Reynolds number $Re_h = Vh/\nu$, where ν represents the kinematic viscosity. The building drag coefficient is scaled by the projected area of solid barriers as follows, $c_D^b = \frac{1}{2} c_D^o a_f h$ where a_f represents frontal area (Nepf, 1999). The units of a_f are length^{-1}, corresponding to the frontal width of obstructions in Ω normalized by Ω. c_D^o is classical drag coefficient that accounts for shape and Reynolds number effects on drag (Sanders et al., 2008).

2.3. Numerical methods

The integral porosity model is solved using a Godunov-based finite volume scheme that allows for triangular, quadrilateral, or mixed meshes (Kim et al., 2014). The scheme uses Roe's approximate Riemann solver with a critical flow fix, an adaptive method of variable reconstruction for uneven topography that minimizes numerical dissipation (Begnudelli et al., 2008), a local time stepping scheme (Sanders, 2008), an improved Volume-Free Surface-Reconstruction (VFR) technique for wetting and drying, and inclusion of grid based porosity parameters (Sanders et al., 2008) which is of particular interest here. The scheme is explicit and conditionally stable in accordance with a CFL condition (Kim et al., 2014).

2.4. Laboratory experiment

Laboratory-scale modeling of anisotropic blockage effects was carried out in a physical model constructed at the Korea Institute of Construction Technology (KICT). Fig. 1(a) and (b) shows the plan view and side view of the physical model, respectively, and Fig. 1(c) shows the location of gage stations and blocks. The experimental tank is 30 × 30 m and includes a reservoir, a dam, and a floodplain. The width and length of the reservoir are 5 m and 30 m, respectively, and the width and length of the floodplain are 28 m and 24 m, respectively (Yoon, 2007).

The reservoir and floodplain surfaces are horizontal and treated with mortar to achieve a uniform roughness. The floodplain is vertically offset 0.4 m above the reservoir, and the two areas are separated by a concrete wall with a sliding gate that is opened horizontally and symmetrically to simulate a breach. The gate moves along a rail set equal in height to the floodplain. To initiate a flood, the sliding gate opens at a velocity of 0.18 m/s until the breach reaches a maximum width of 1.0 m. At the outer boundary of the model floodplain, there is a vertical drop of 0.4 m into a

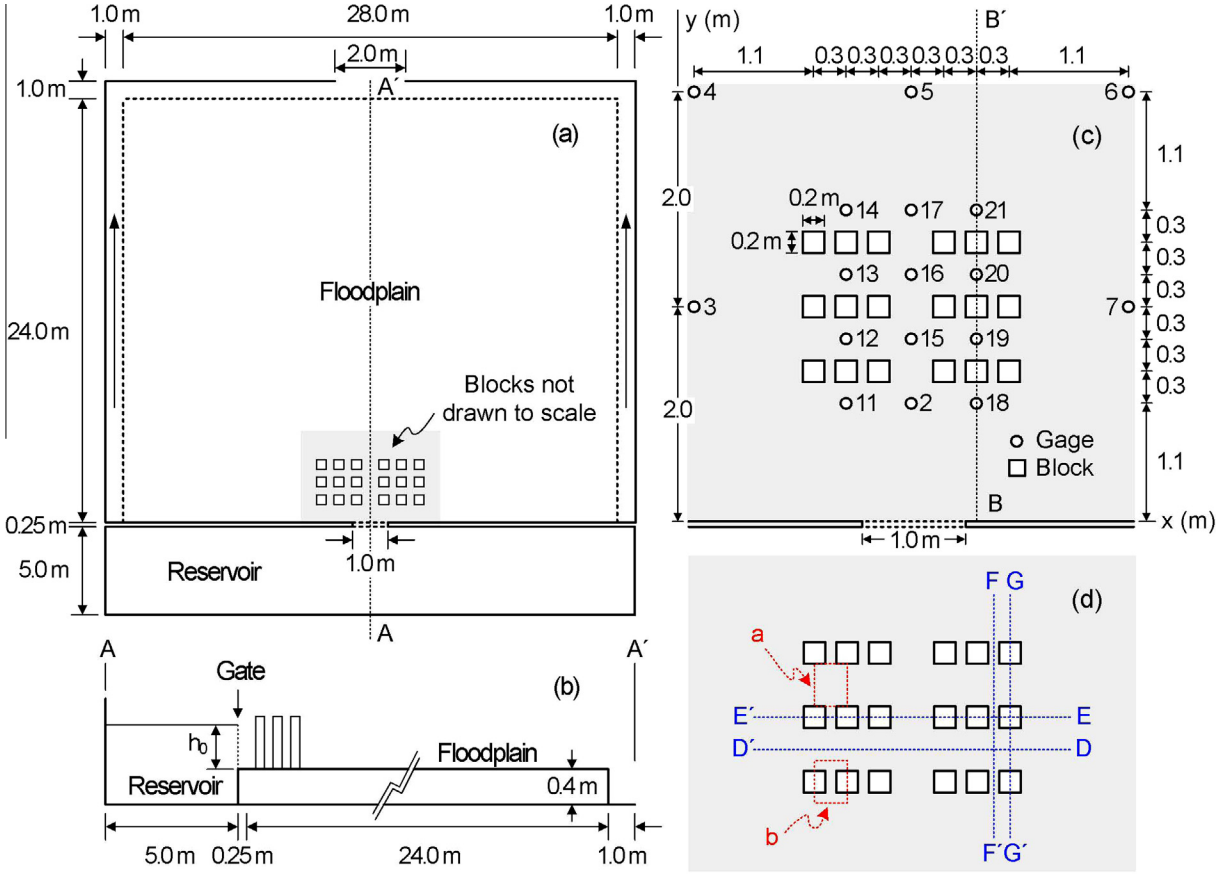

Fig. 1. Experiment set-up of Yoon (Yoon, 2007): (a) plan view, (b) side view, and (c) close-up of greyed section in Fig. 1(a); and (d) cell-based porosity ϕ exhibits heterogeneity depending on control volume placement, a vs. b, and edge-based porosities ψ exhibit heterogeneity and anisotropy depending on the chosen transect.

channel 1.0 m wide for drainage. The floodplain and perimeter drainage channel were designed to ensure a free-outflow condition along the entire perimeter. The solid blocks are 0.2 × 0.2 m square pillars made of an acrylic shell and filled with concrete for stability during flood conditions. The blocks were arranged as two 3 × 3 groups that are symmetrically aligned about the centerline of the dam as shown in Fig. 1 (Yoon, 2007).

A total of 17 capacitance-type gages (Model CHT4-60, KENEK, Tokyo, Japan) were installed to measure transient flow depths as shown in Fig. 1(c). The probes measured depths in the range 0–30 cm and sampled at a rate of 5 Hz (0.2 s sampling interval). It is noted that several stations are positioned as symmetric pairs about the dam centerline as shown in Fig. 1(c). Two different flow scenarios are considered corresponding to an initial reservoir water depth (h_0) of 0.30 m and 0.45 m, measured relative to the floodplain elevation (Yoon, 2007).

Within each 3 × 3 cluster, the gap between buildings is 0.1 m facing the dam (section E–E′ in Fig. 1(d)) and 0.4 m perpendicular to the dam (section G–G′ in Fig. 1(d)). This introduces a strong degree of anisotropy in the porosity field, a 1–4 ratio in the cross-sectional area available for flow between blocks. The KICT problem also introduces pore-scale heterogeneity in the porosity distribution. For example, considering again Fig. 1(d), the areal porosity ψ varies significantly between Sections D–D′ and E–E′ in the y direction, with $\psi_E < \psi_D$, and between Sections G–G′ and F–F′ in the x direction, with $\psi_G < \psi_F$. Similarly, the volumetric porosity ϕ varies significantly between domain a and b shown in Fig. 1(d), with $\phi_b < \phi_a$.

2.5. Summary of models

A classical shallow-water model (CSW), the anisotropic porosity model (PSW-A), and four isotropic porosity models (PSW-I) were applied. Additionally, results of the classical shallow-water model were averaged over each porosity-model grid cell to yield a pore-scale classical shallow-water model result (CSW-P). Table 1 presents a summary of the seven models, and Fig. 2 presents the computational meshes used. Note that Fig. 2(b) corresponds to the gap-conforming mesh required of the anisotropic model (Sanders et al., 2008), where vertices are placed at the centroid of obstructions, cells are aligned with pore spaces, and edges intersect constrictions in the pore space. Additionally, Fig. 2(c) corresponds to a region conforming mesh that precisely circumscribes the subdomain filled with flow barriers (Soares-Frazão et al., 2008; Guinot, 2012). Four variants of the isotropic porosity model are used to account for both mesh designs and two alternative porosity values corresponding to the region-averaged volumetric porosity (Soares-Frazão et al., 2008) and the areal porosity (Guinot, 2012), as shown in Table 1. It is noted that an REV cannot be rigorously established in this test case due to the anisotropy, heterogeneity and limited spatial extent of the flow barriers, so the assumptions required to apply the isotropic model are not satisfied. However, isotropic models have yielded credible yet less accurate predictions (than anisotropic models) in other applications where these requirements were not satisfied (Guinot, 2012), motivating further study here.

2.6. Definition of errors

Three types of errors are reported: (a) structural model errors, (b) scale errors and (c) porosity model errors. Structural model errors are defined by the difference between the converged CSW prediction and gage measurements of flood depths. Scale errors are defined by the difference between the CSW (point scale) and CSW-P (pore scale) predictions at gage locations, and are computed for both depth and velocity. Porosity model errors are defined by the difference between porosity model predictions and CSW-P at gage locations (pore scale comparison), and are evaluated for both depth and velocity. All errors are computed using an L_1 norm defined by $L_1 = \sum_{j=1}^{N} |(w_1)_j - (w_2)_j|/N$ where w_1 and w_2 represent

Table 1
Shallow-water model formulations and corresponding meshes shown in Fig. 2.

Case0	Description	Mesh in Fig. 2	Num. of nodes	Num. of cells	Resolution (m)		
					Avg.	Max.	Min.
CSW	Classical shallow-water	(a)	330,464	328,612	0.05	0.05	0.05
CSW-P	Pore-scale average of CSW	(a)	330,464	328,612	0.05	0.05	0.05
PSW-A	Anisotropic porosity model	(b)	9216	8932	0.30	0.33	0.25
PSW-I-1A	Isotropic porosity model ($\phi = \psi = 0.74$)	(c)	9412	9124	0.30	0.33	0.25
PSW-I-1B	Isotropic porosity model ($\phi = \psi = 0.40$)	(c)	9412	9124	0.30	0.33	0.25
PSW-I-2A	Isotropic porosity model ($\phi = \psi = 0.83$)	(b)	9216	8932	0.30	0.33	0.25
PSW-I-2B	Isotropic porosity model ($\phi = \psi = 0.50$)	(b)	9216	8932	0.30	0.33	0.25

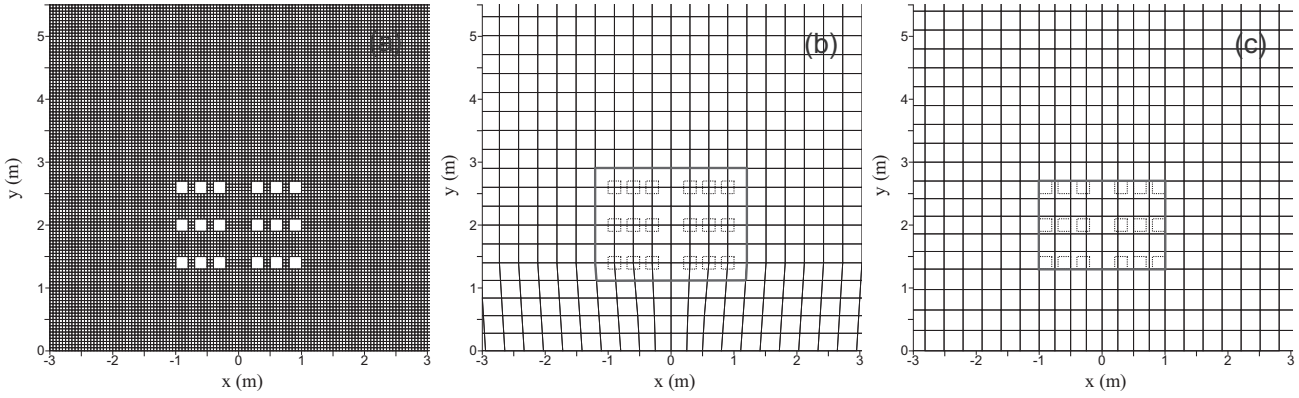

Fig. 2. Computational mesh for (a) CSW and CSW-P, (b) PSW-A, PSW-I-2A and PSW-I-2B, and (c) PSW-I-1A and PSW-I-1B.

the two different solutions and N represents the number of points compared.

2.7. Model parameterization and calibration

For all models, mesh vertex heights were assigned based on reservoir or floodplain bed elevations, and mesh cells were assigned a Nikuradse sand-grain roughness height k_s to model bottom shear. Further, a no-normal-flux boundary condition was enforced along the reservoir boundaries and concrete wall separating the reservoir and floodplain, and a free-outflow boundary condition was enforced along the remaining three sides of the floodplain. The gate opening was modeled as an instantaneous breach since the time scale of opening (<3 s) is short compared with the time-scale of the breach flow (>100 s).

To apply the anisotropic porosity model, the cell-based porosity ϕ_j and edge-based porosity ψ_k were computed based on the intersection of the mesh with the footprint of the solid blocks following previously described methods (Sanders et al., 2008; Schubert and Sanders, 2012). Additionally, the frontal area parameter a_f required to parameterize drag was computed on a cell-by-cell basis in accordance with the projected area facing the dam as described previously (Sanders et al., 2008). The assumption of a uniform flow direction for computing a_f is an approximation that has worked reasonable well in practical applications (Schubert and Sanders, 2012).

To apply the isotropic porosity models, ϕ_j and ψ_k were assigned a uniform value inside the block zone. Referring to Table 1, PSW-I-1A and PSW-I-2A are based on an average volumetric porosity corresponding to the spatial extent of cells that contact the obstructions, and the porosity values differ slightly based on the mesh. PSW-I-1B and PSW-I-2B are based on areal porosity values corresponding to transect E–E′ in Fig. 1(d). A uniform frontal area parameter was also specified inside the block zone equal to the total frontal area facing the dam, normalized by the size of the block zone. This corresponds to 0.83 and 1.29 m^{-1} (Table 1) for the meshes shown Fig. 2(b) and (c), respectively.

Outside the block zone, a porosity value of unity was assigned in all porosity models. Also, the frontal area was set to zero.

The roughness parameter, k_s, was manually calibrated by applying CSW to the first KICT flow scenario (h_0 = 0.30 m) with k_s values ranging from 0.03 to 0.3 cm, which is an established range for concrete (Munson et al., 2006). The k_s value achieving the best agreement between predicted depths and gage measurements (minimum L_1 norm) was subsequently used in all other models and in the second KICT flow scenario (h_0 = 0.45 m).

To calibrate c_D^o, each of the porosity models was applied to the first KICT flow scenario with c_D^o values ranging from 1.0 to 3.0. This range corresponds to rectangular shaped blocks in an idealized two-dimensional flow (Munson et al., 2006), and it is recognized that c_D^o may also vary depending on sheltering effects from the clustering of solid barriers and three-dimensional flow effects (Sanders et al., 2008).

When calibrating c_D^o, a critical question is which reference solution to use for measuring the error (L_1 norm). Calibration to gage measurements is the first option and is motivated by the goal of minimizing the overall error in the porosity model prediction, whereas another option is calibration to CSW-P predictions which is motivated by the goal of minimizing porosity model errors. Further, calibration to CSW-P depth and/or velocity predictions is possible. Here, all three options are pursued leading to three different calibrations: calibration to depth measurements (Calib1), calibration to CSW-P predictions of depth at gage locations (Calib2), and calibration to CSW-P predictions of velocity at gage locations (Calib3).

3. Results

3.1. Convergence of the CSW model

A resolution of 0.05 m was selected for CSW after a convergence check with a 0.025 m mesh of approximately 1.3 million computational cells. This showed that the average convergence error (measured over the simulation period at each gage) of the CSW depth prediction was less than 2 mm at all stations except Gage 2, where the convergence error was found to be 6 mm. Over all stations, the average convergence error was approximately 1 mm. Gage 2 is located in front of the leading row of obstructions (see Fig. 1). Here, super-critical flow through the breach strikes the first row of blocks, and a bow shock (hydraulic jump) forms across the width of the blocks as shown in Fig. 3. Based on the curvature of the shock wave, Gage 2 is on the windward side of the shock and Gages 11 and 18 are on the leeward side. Further, the width of the shock wave (measured in y direction on Fig. 3) is minimal at Gage 2: over a distance of 30 cm in the y direction, the water depth rises up from 5 cm to 16 cm, and then down again to 10 cm, approximately, based on results shown in Fig. 3(b). As the mesh is coarsened from 0.025 to 0.05 m resolution, this narrow band of super-elevated water is diffused slightly and its windward edge moves closer to Gage 2, leading to higher water depth predictions. Hence, the relatively large convergence error at Gage 2 is explained by its position at the leading edge of a shock wave. It is noted that porosity models use a 30 cm mesh resolution (Fig. 2(c) and (d), and

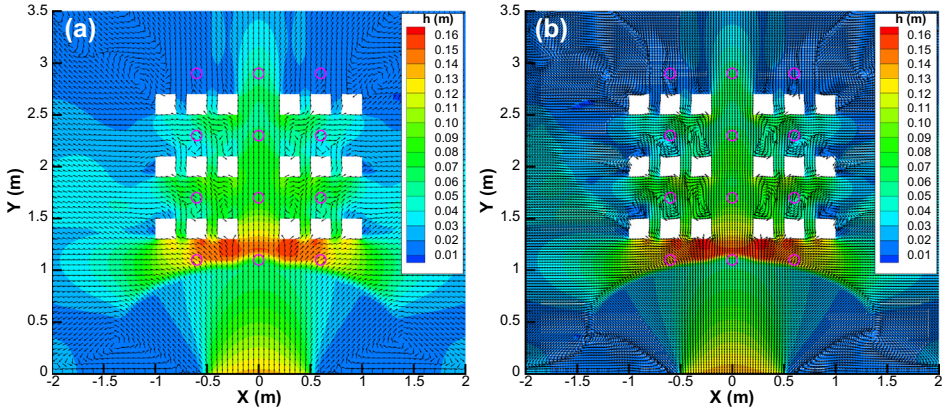

Fig. 3. Contours of water depth 50 s after dam-break on CSW-S with (a) 0.05 m and (b) 0.025 m resolution. Vectors indicate velocity direction.

Table 1), which is too coarse to sharply resolve the narrow band of super-elevated water at Gage 2. This shows that pore-scale and point-scale values of flood predictions may differ substantially as a result of localized wakes and wave reflections from flow obstructions.

3.2. Calibration of k_s

Fig. 4 shows CSW model predictions of depth using k_s values from 0.03 to 0.3 cm, compared with gage measurements. Additionally, Table 2 shows L_1 norms for CSW model. These results demonstrate that the influence of roughness depends on the gage location, but overall roughness does not exhibit a strong influence on the average error. The implication is that momentum losses are dominated by the geometric constriction and form drag associated with the solid blocks, not skin friction from the bottom boundary. All subsequent modeling uses k_s = 0.03 cm since this leads to the most accurate prediction based on the values considered.

3.3. Calibration of c_D^o

Table 3 presents L_1 norms in porosity model predictions as a function of c_D^o and different reference solutions. This shows that optimal c_D^o depends on the porosity model and also depends on whether the goal is to minimize total errors or porosity model errors. In four of the five models, minimizing porosity model errors calls for a drag coefficient on the low end of the range (1.0) while minimizing total errors calls for a drag coefficient at the high end of the range (3.0). We conjecture that the goal of a porosity model should be to reproduce as accurately as possible the pore-scale

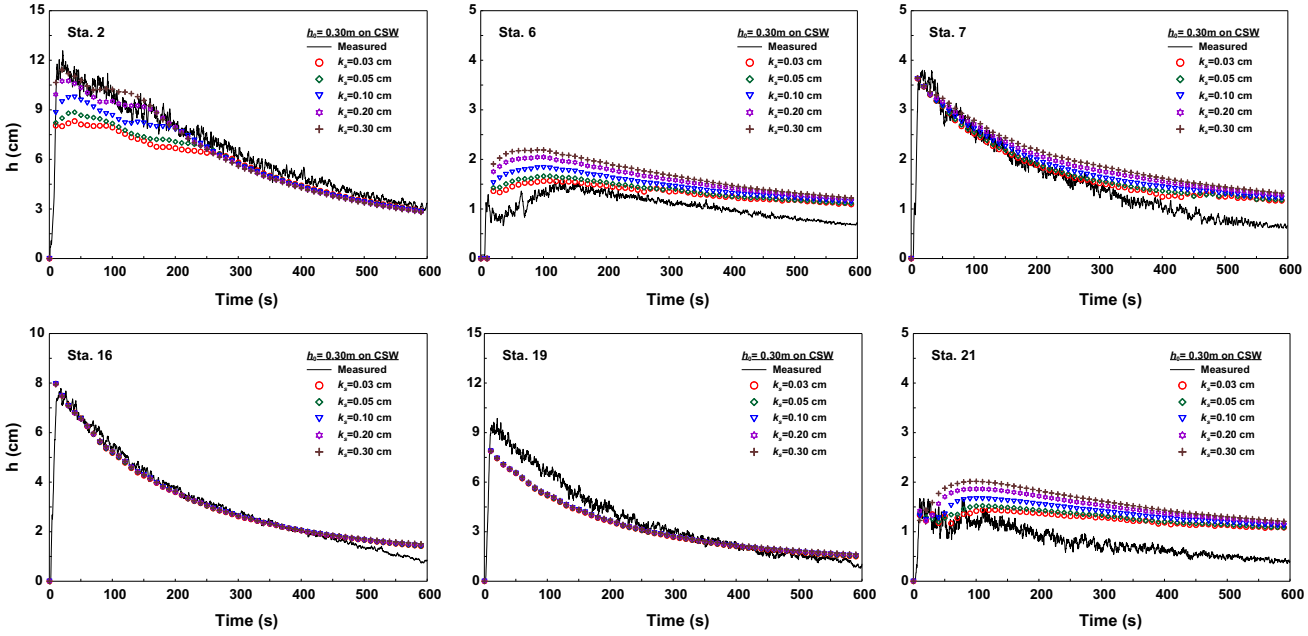

Fig. 4. Flood depth sensitivity to roughness height (k_s) on CSW.

Table 2
L_1 norms of flood depth for calibration of roughness height (k_s) on CSW (unit: cm).

Case	k_s (cm)	Gages inside block zone									Gages outside block zone				Entire avg.
		2	11&18	12&19	13&20	14&21	15	16	17	Avg.	3&7	4&6	5	Avg.	
CSW	**0.03**	1.08	1.22	0.66	0.44	0.58	1.49	0.23	0.29	0.75	0.33	0.39	0.81	0.51	0.63
	0.05	0.94	1.23	0.66	0.44	0.62	1.49	0.23	0.29	0.74	0.35	0.44	0.82	0.54	0.64
	0.10	0.71	1.24	0.66	0.44	0.70	1.48	0.23	0.29	0.72	0.40	0.53	0.89	0.61	0.66
	0.20	0.56	1.25	0.66	0.45	0.83	1.46	0.23	0.30	0.72	0.49	0.66	1.03	0.72	0.72
	0.30	0.57	1.26	0.67	0.46	0.91	1.44	0.23	0.30	0.73	0.56	0.74	1.12	0.81	0.77

Bold values show the minimum L_1 norm from the c_D^o values considered.

Table 3
L_1 norms of flood depth for calibration of drag coefficient (c_D^o) on PSW-A and PSW-I.

Case	L_1 of flood depth (unit: cm) Calib1: Ref.-Measured h					L_1 of flood depth (unit: cm) Calib2: Ref.-Predicted h on CSW-P					L_1 of flood velocity (unit: cm/s) Calib3: Ref.-Predicted V on CSW-P				
	$c_D^o = 1.0$	1.5	2.0	2.5	3.0	$c_D^o = 1.0$	1.5	2.0	2.5	3.0	$c_D^o = 1.0$	1.5	2.0	2.5	3.0
PSW-A	0.705	0.681	0.669	0.663	**0.660**	**0.165**	0.186	0.21	0.231	0.248	**10.958**	11.816	12.513	13.111	13.695
PSW-I-1A	1.068	1.021	1.015	1.012	**1.003**	**0.507**	0.545	0.578	0.592	0.590	**21.730**	21.893	22.132	22.136	21.960
PSW-I-1B	0.751	0.732	**0.726**	0.728	0.732	**0.337**	0.387	0.422	0.446	0.464	**21.581**	21.812	21.956	22.123	22.171
PSW-I-2A	1.152	1.088	1.04	1.003	**0.974**	0.601	**0.529**	0.533	0.543	0.533	22.084	21.05	20.798	20.505	**20.142**
PSW-I-2B	0.815	0.78	0.761	0.752	**0.749**	**0.278**	0.284	0.317	0.341	0.360	20.532	20.343	20.204	20.152	**20.122**

Bold values show the minimum L_1 norm from the c_D^o values considered.

averaged solution of the shallow-water equations, and not necessary match measurements. However, the results here clearly indicate that c_D^o can be tuned to improve the agreement with measurements.

The calibrations also show that over a range of physically realistic drag coefficient values, the anisotropic model consistently produces smaller total errors and porosity model errors in flood depths.

Table 4
Model parameters and run time.

Case	k_s (cm)	C_D^o			ϕ	ψ	a_f (m^{-1})	Max. *Cr.*	h_0 = 0.30 m		h_0 = 0.45 m	
		Calib1	Calib2	Calib3					Δt(s)	Runtime (s)	Δt(s)	Runtime (s)
CSW	0.03	–	–	–	–	–	–	0.6	0.0079	5699	0.0062	7264
CSW-P	0.03	–	–	–	–	–	–	0.6	0.0079	5699	0.0062	7264
PSW-A	0.03	3.0	1.0	1.0	0.76–0.89	0.33–0.67	1.09–2.38	0.6	0.0565	9.34	0.0460	11.34
PSW-I-1A	0.03	3.0	1.0	1.0	0.74	0.74	1.29	0.6	0.0563	9.45	0.0460	11.58
PSW-I-1B	0.03	2.0	1.0	1.0	0.40	0.40	1.29	0.6	0.0563	9.45	0.0460	11.53
PSW-I-2A	0.03	3.0	1.5	3.0	0.83	0.83	0.83	0.6	0.0564	9.38	0.0460	11.28
PSW-I-2B	0.03	3.0	1.0	3.0	0.50	0.50	0.83	0.6	0.0564	9.39	0.0460	11.25

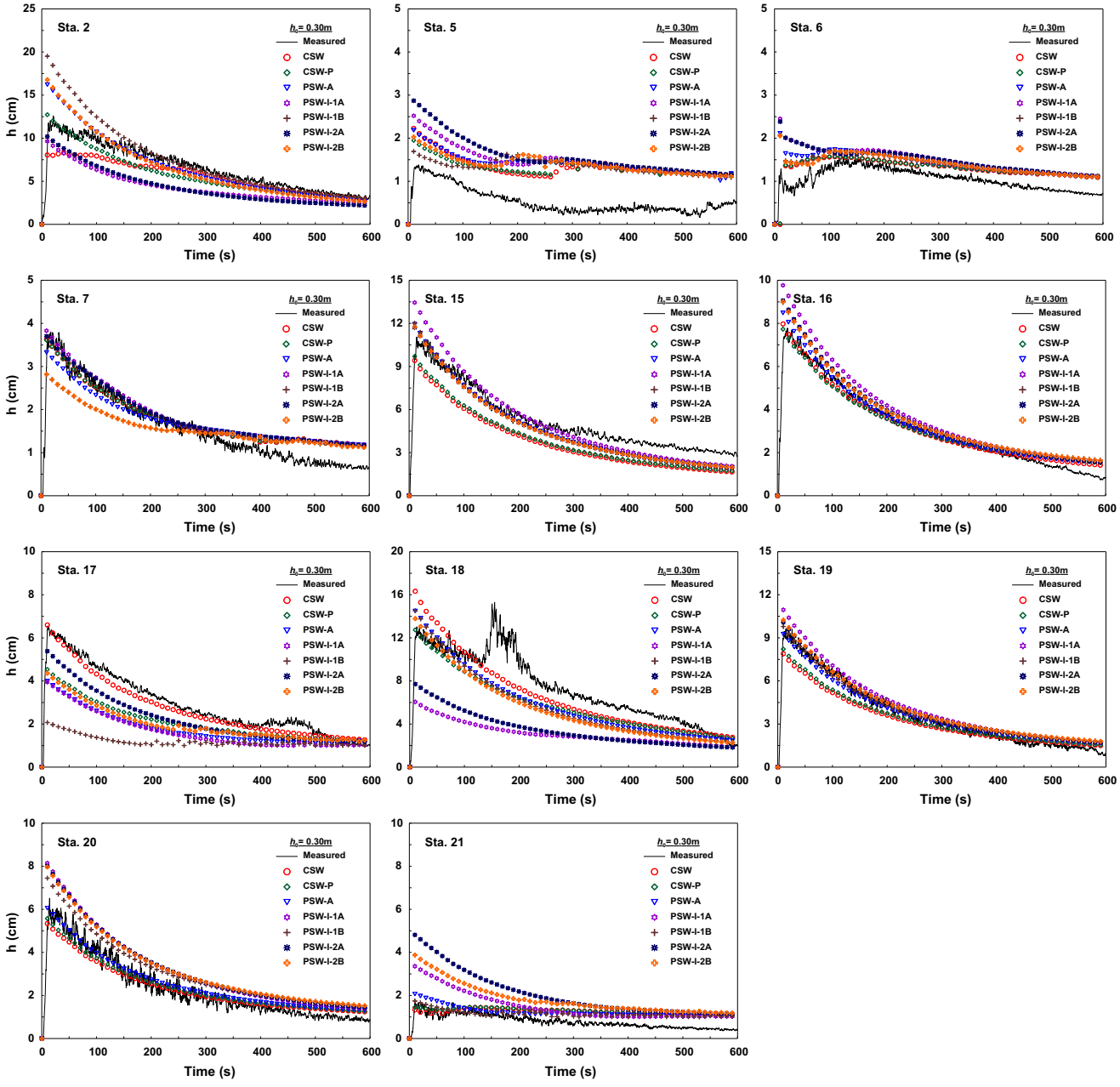

Fig. 5. Comparison of predicted flood depth and measurement for h_0 = 0.30 m.

3.4. Model predictions and errors

Table 4 provides a summary of all model configurations and run times, including optional parameter values corresponding to different calibrations. Models were executed using a 3.07 GHz Intel® Core™ i7 CPU with 8 GB RAM. The differences in run time are striking as in previous studies. Compared with CSW, the porosity models execute almost three orders of magnitude faster.

Figs. 5 and 6 present predictions and gage measurements of flood depth for the first (h_0 = 0.30 m) and second (h_0 = 0.45 m) test cases based on Calib1, and Figs. 7 and 8 present model predictions of velocity for the first and second test cases based on Calib1. Results from Calib2 and 3 are not shown graphically, but Table 5 shows L_1 norms according to the porosity model, the calibration, and the reference solution. L_1 norms based on flood depth measurements are used to measure the structural model error in the CSW model and the total error in the porosity models, while L_1 norms based on the CSW-P prediction are used to measure porosity model errors. The scale error is measured by an L_1 norm between the CSW and CSW-P predictions.

3.4.1. Structural model errors

The CSW prediction is shown to yield a good approximation of flood depths across the spatial domain (Fig. 5), with an average error of only 0.63 cm (Table 5), which represents just 2% of the initial depth in the reservoir. The main limitations of CSW are noted at Sta. 18 where a spurious wave is measured in the experiment that is not explained by the model, and at Sta. 5 where the model overpredicts flood depths roughly by a factor of two. In a second test case involving h_0 = 0.45 m (Fig. 6), the average error is 0.89 cm (Table 5) which is again just 2% of the initial depth in the reservoir. Hence, after calibration of the model to the first test

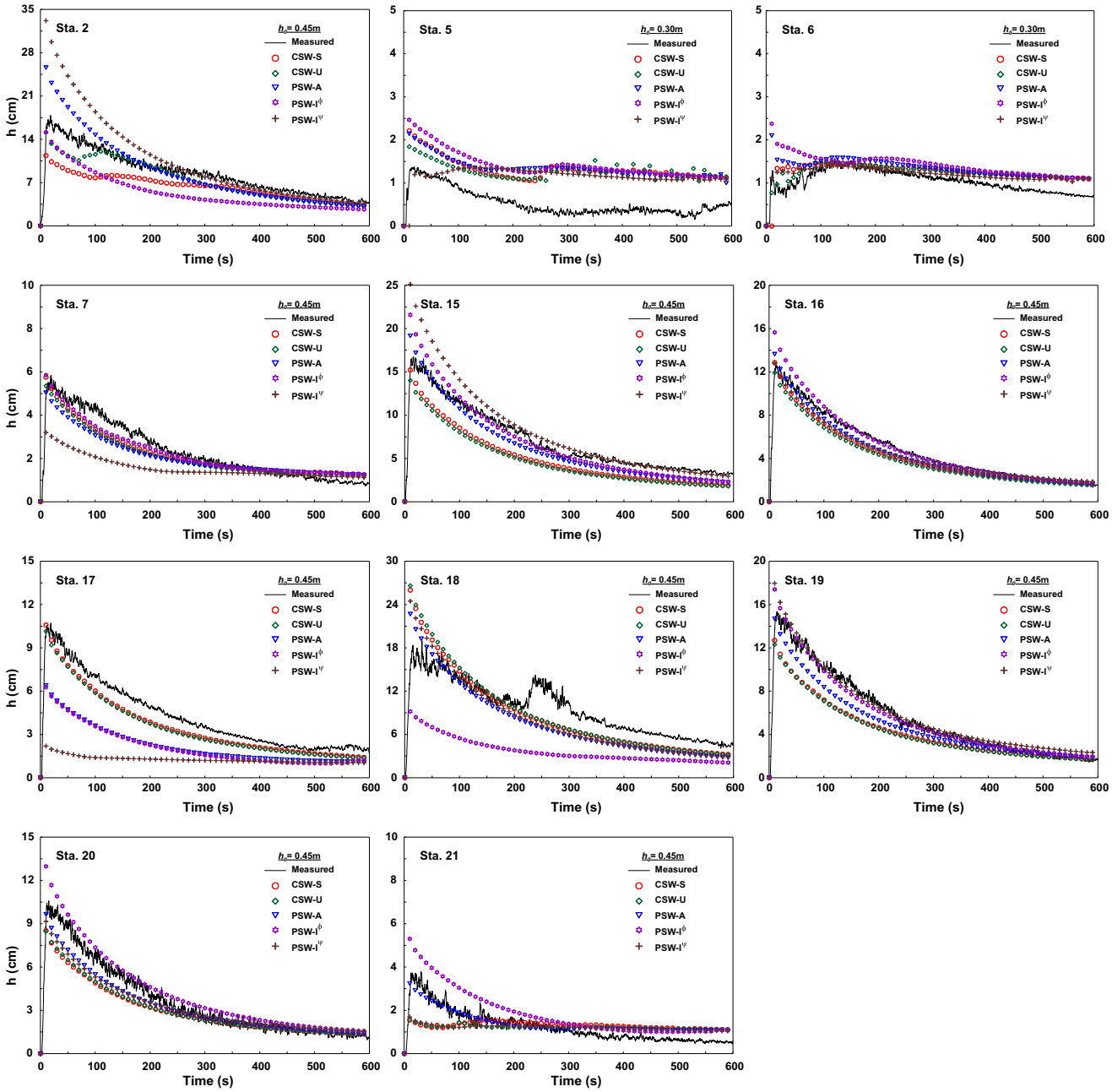

Fig. 6. Comparison of predicted flood depth and measurement for h_0 = 0.45 m.

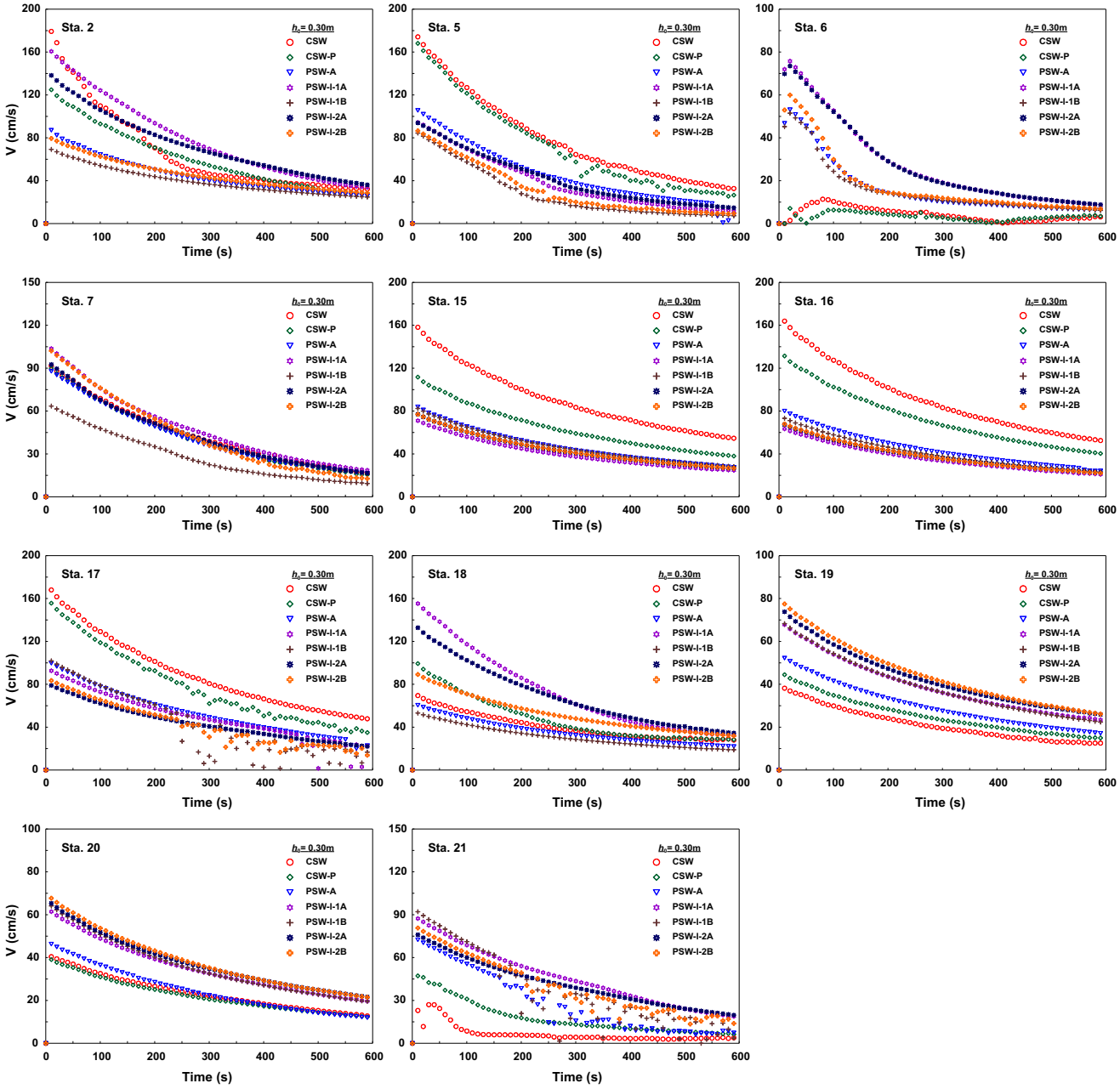

Fig. 7. Comparison of predicted flood velocity for h_0 = 0.30 m.

case, the model performs with the same relative error in a second test case.

3.4.2. Scale errors

Differences between point-scale (CSW) predictions and pore-scale (CSW-P) predictions of flood depth constitute the scale error which is at least 65% smaller than the structural model error according to L_1 norms shown in Table 5. In particular, the scale error in depth is 0.18 cm in the first test case where the structural model error is 0.63 cm. In the second test case, the scale error is 0.30 cm while the structural model error is 0.89 cm. Table 5 also shows that the scale error in velocity is 7.45 and 9.12 cm/s, which corresponds to about 2% of the theoretical peak velocity of a dry-bed dam break flood wave, $2(gh_0)^{1/2}$.

Figs. 5 and 6 illuminate the origin of the scale error. In the first test case (Fig. 5), CSW-P notably departs from CSW at Sta. 2 which is explained by the shock waves shown in Fig. 3. This occurs because at the point scale, the prediction corresponds to one side of the shock or the other, while at the pore scale, the prediction corresponds to a spatial average around the shock. Noticeable differences also occur at two other stations on the perimeter of the obstructions (e.g., Sta. 17 and 18), while differences away from the obstructions (Sta. 5, 6, and 7) and at stations off center from the main flow path (Sta. 19 and 20) are minimal.

Differences between the point-scale and pore-scale velocities in Figs. 7 and 8 are noted at Sta. 2, 15 and 16 where relatively high velocities occur due to the alignment of this channel with the dam-break flood wave. Here, faster velocities occur along the centerline and slower velocities occur near the blocks as a result of wakes, and the monitoring stations sample the fastest moving water. Relatively large scale effects are also noted at Sta. 18 and 21.

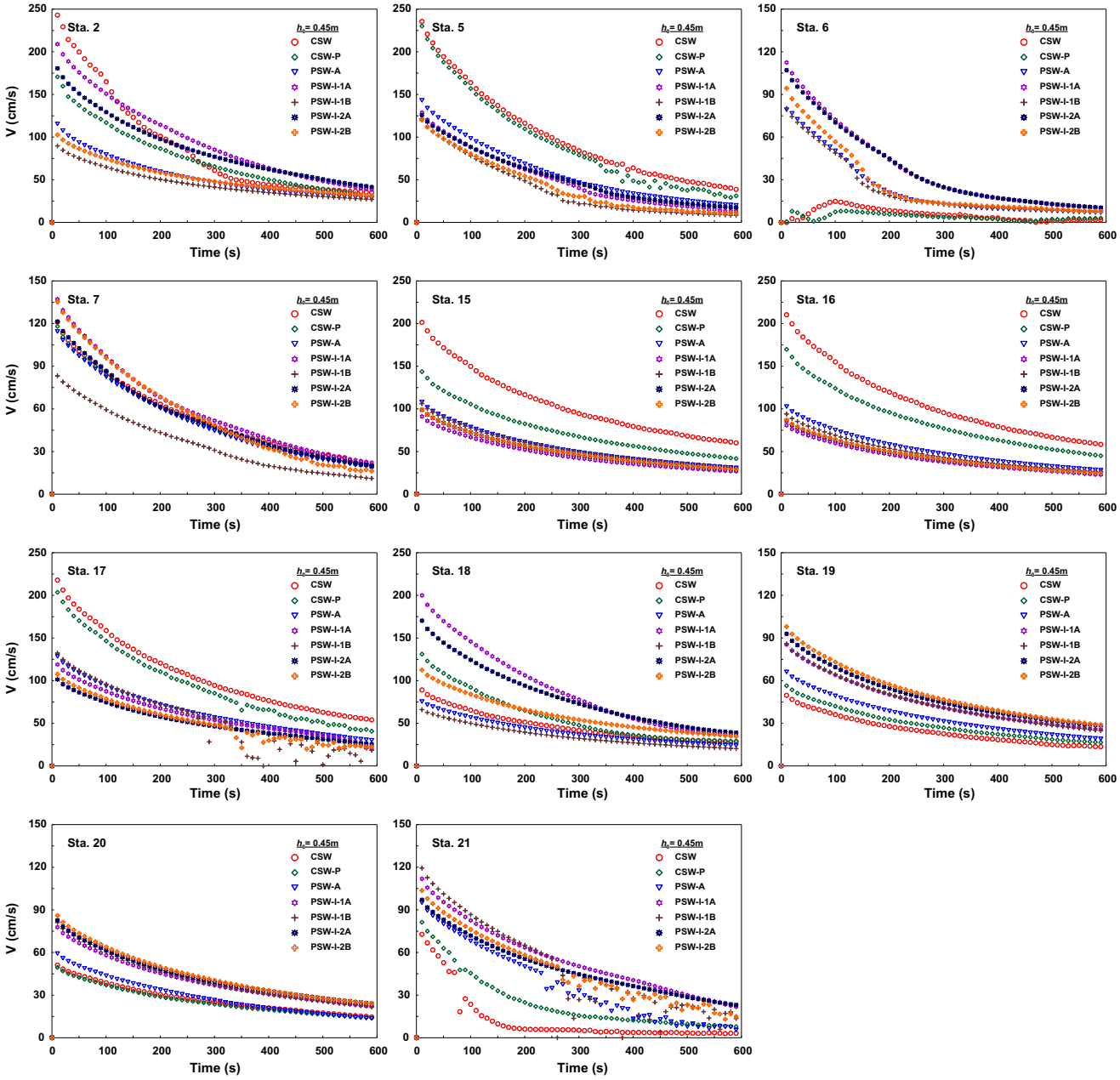

Fig. 8. Comparison of predicted flood velocity for h_0 = 0.45 m.

3.4.3. Porosity model errors

Attention is now focused on porosity model errors in flood depth and velocity, which are measured by a comparison of porosity model predictions and CSW-P. Table 5 shows that the anisotropic porosity model introduces a significantly smaller error in depth and velocity than all of the isotropic porosity models. For example, in the first and second test cases, isotropic model errors in depth were 65–210% and 77–240% greater than the anisotropic model, respectively, based on Calib2. Additionally, isotropic model errors in velocity were 83–97% and 80–86% greater than the anisotropic model for the first and second test cases, respectively, based on Calib3. Data in Table 5 also shows that the magnitude of the porosity model errors is mostly greater than or equal to the scale error, but less than the structural model errors, for both depth and velocity. The exception is the second test case where the anisotropic porosity model errors in depth are actually smaller than the scale error.

The total error of the porosity models at the point scale is also shown in Table 5, with L_1 norms based on gage depth measurements. The total errors of the anisotropic porosity model are nearly identical to CSW and CSW-P based on Calib1, while all of the isotropic models yield larger total errors. Errors in the isotropic models range from 16% to 59% higher than CSW errors in the first test case, and 2–29% higher in the second test case, based on Calib1.

3.5. Spatial variability

Previously shown results reveal at-a-station dynamics, but it is also worthwhile to examine the spatial structure of flood predictions. For the h_0 = 0.30 m case, Fig. 9 shows contours of pore-scale flood depth and vectors representing the pore-scale velocity magnitude and direction 50 s after the dam-break as depicted by:

Table 5
L_1 norms of flood depth and velocity based on calibration and reference solution.

h_0 (m)	Case	L_1 of flood depth (unit: cm) Ref.-Measured h			L_1 of flood depth (unit: cm) Ref.-Predicted h on CSW-P			L_1 of flood velocity (unit: cm/s) Ref.-Predicted V on CSW-P		
		Calib1	Calib2	Calib3	Calib1	Calib2	Calib3	Calib1	Calib2	Calib3
0.30	CSW	0.63	0.63	0.63	0.18	0.18	0.18	7.45	7.45	7.45
	CSW-P	0.66	0.66	0.66	–	–	–	–	–	–
	PSW-A	0.66	0.70	0.70	0.25	0.17	0.17	13.70	10.96	10.96
	PSW-I-1A	1.00	1.07	1.07	0.59	0.51	0.51	21.96	21.73	21.73
	PSW-I-1B	0.73	0.75	0.75	0.42	0.34	0.34	21.93	21.58	21.58
	PSW-I-2A	0.97	1.09	0.97	0.53	0.53	0.53	20.14	21.05	20.14
	PSW-I-2B	0.75	0.81	0.75	0.36	0.28	0.36	20.12	20.53	20.12
0.45	CSW	0.89	0.89	0.89	0.30	0.30	0.30	9.12	9.12	9.12
	CSW-P	0.89	0.89	0.89	–	–	–	–	–	–
	PSW-A	0.87	0.91	0.91	0.36	0.22	0.22	17.90	14.35	14.35
	PSW-I-1A	1.15	1.39	1.39	0.81	0.71	0.71	27.46	28.16	28.16
	PSW-I-1B	0.95	1.05	1.05	0.62	0.50	0.50	27.29	27.27	27.27
	PSW-I-2A	1.15	1.40	1.15	0.73	0.74	0.73	25.04	26.32	25.04
	PSW-I-2B	0.91	1.12	0.91	0.52	0.39	0.52	25.35	25.78	25.35

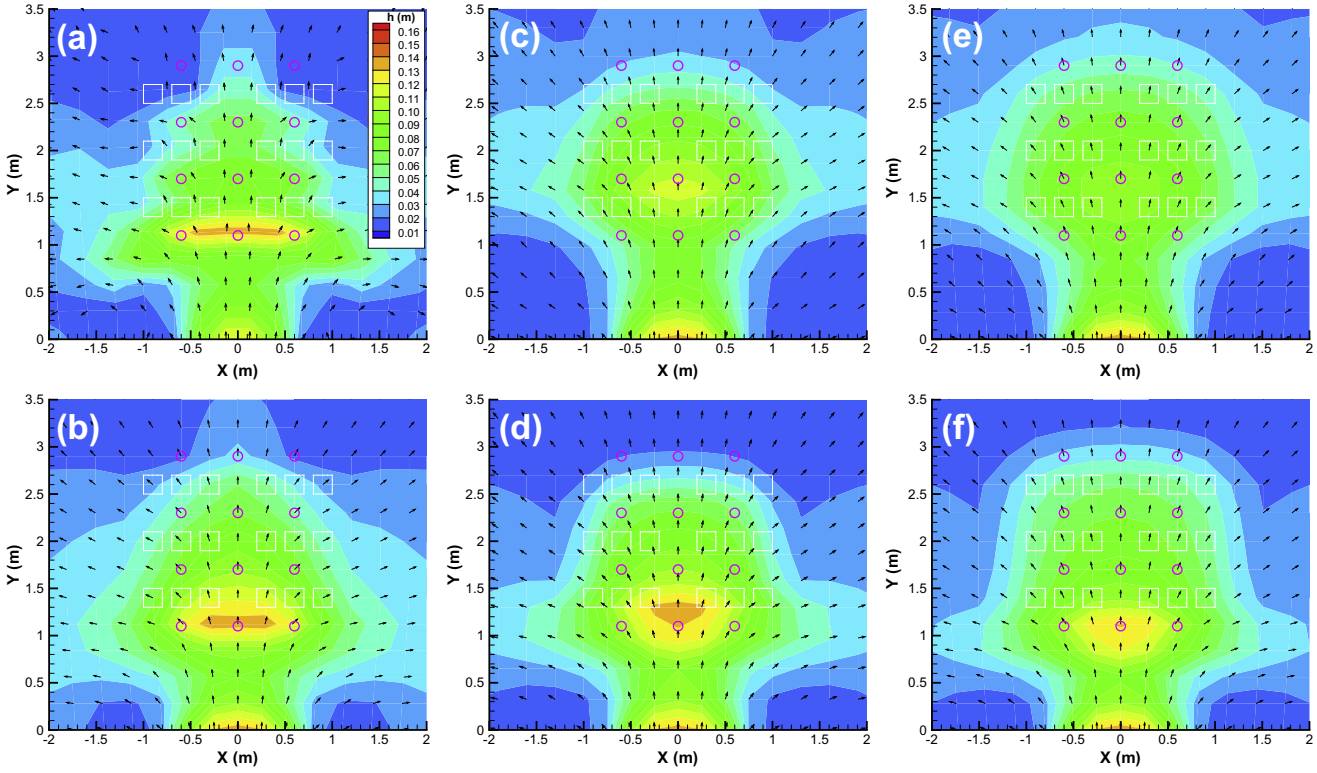

Fig. 9. Contours of water depth 50 s after dam-break on (a) CSW-P, (b) PSW-A, (c) PSW-I-1A, (d) PSW-I-1B, (e) PSW-I-2A and (f) PSW-I-2B. Vectors indicate velocity direction.

(Fig. 9(a)) CSW-P, (Fig. 9(b)) PSW-A, and (Fig. 9(c)–(f)) the four isotropic porosity models. CSW-P predicts a zone of elevated water (region colored green, yellow and red) that approximates a triangular shape, and this shape is retained fairly well by PSW-A, but not as well by the isotropic models. The isotropic models predict a more rounded shape which reflects a lack of directionality. Focusing on the bow shock in front of the obstructions, the CSW-P and PSW-A predict a laterally distorted shape, while the isotropic models predict a more rounded shape, again reflecting a lack of directionality.

Fig. 10 shows the flood depth distribution for the $h_0 = 0.30$ m case at four successive times along the transects through the block zone labeled B–B′ in Fig. 1(c), as depicted by point-scale measurements, CSW, CSW-P, and the porosity models. CSW, CSW-P and PSW-A show the formation of a bow shock 1 m from the dam and immediately upstream of the first block, and an adverse free surface slope upstream of the second and third block from the dam. On the other hand, the isotropic porosity models fail to capture this depth variability and instead predict a relatively smooth variation of the flood depth through the block zone. This is a result of using a uniform porosity value through the region of obstacles, and consistent with the design of isotropic models to predict flow properties at the REV scale which is considerably larger than the pore scale. Figs. 9 and 10 also reveal insight into the sensitivity of isotropic porosity models to the porosity value. Generally, with a decrease in the porosity value, the height of the bow shock increases and it shifts forwards towards the dam.

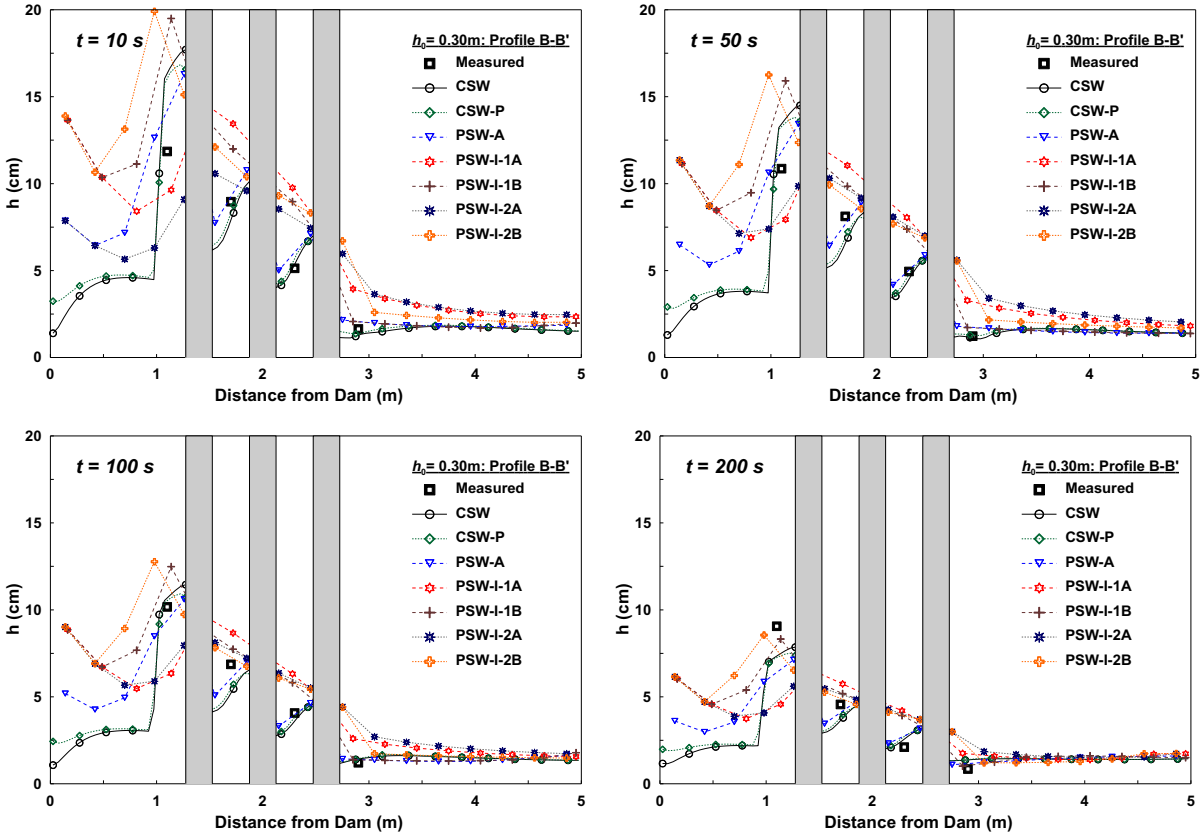

Fig. 10. Profile of flood depth after dam-break for h_0 = 0.30 m at B–B′ in Fig. 1(c).

4. Discussion

The preceding results show that porosity model errors may be significantly larger than scale errors which pose an opportunity for improved porosity models. The margin for improvement of the anisotropic model relative to flood depths is small, but the potential for improvement of the velocity predictions is greater and motivates improved models of flow resistance, possibly allowing for more spatial variability in parameters, or even fundamentally new approaches or more advanced calibration procedures. However, research directed at improving porosity model formulations should be mindful of structural model errors. Based on the data presented here, the anisotropic model is equally accurate as the point-scale classical shallow-water model relative to flood depth prediction, so further reduction in porosity model errors cannot be expected to reduce total errors. Broadly, porosity models cannot be expected to predict flood depths any more accurately than the pore-scale average of the foundational flow model, in this case the classical shallow-water equations.

There is pressing need for urban flood inundation models that can be efficiently and accurately applied over practical scales such as a city or regional flood plain, and these results and previous studies (Yu and Lane, 2005; McMillan and Brasington, 2007; Soares-Frazão and Zech, 2008; Sanders et al., 2008; Guinot, 2012) reveal great potential for porosity models to address this need. But aside from accuracy, a critical question to address is whether any of the porosity models can be more easily parameterized and validated in practical applications. High quality site data is often available for flood modeling studies but calibration data is rare, so there is a need for flood models with parameters that can be estimated deterministically and relied upon to make accurate predictions. This further supports use of the anisotropic model because porosity parameters are a deterministic function of the flow obstructions (Sanders et al., 2008; Schubert and Sanders, 2012), in contrast with the isotropic model. However, calibration data may still be needed to estimate porosity model drag parameters for the anisotropic model (Schubert and Sanders, 2012, e.g.,). In the less common scenario where high quality site data are not available to guide the porosity specification, but calibration data exists, the isotropic model may be preferred as the porosity value itself can be used as a calibration parameter.

5. Conclusions

Urban flood models based on porous shallow-water equations predict flood depths and velocities with three types of errors: (a) structural model errors associated with the limitations of the 2D shallow-water equations (e.g., hydrostatic pressure, vertical uniform velocity distributions), (b) scale errors associated with use of a relatively coarse, pore-scale grid comparable to the spacing between buildings, and (c) porosity model errors related to the treatment of sub-grid scale obstructions. Results from a unique test case with anisotropy in the porosity distribution, as in practical applications, show that porosity model errors are mostly greater than scale errors but less than structural model errors, although in one test case the porosity model error of the anisotropic model was slightly less than the scale error. Results also show that porosity model errors in depth and velocity are significantly smaller with an anisotropic porosity model compared to isotropic models, and that the anisotropic porosity model is equally accurate as a fine grid shallow-water model, based on the total error. Recognizing that all porosity models reduce run times by a factor of nearly a thousand compared with the classical shallow-water models, the anisotropic porosity model stands out as the most efficient approach for pore-scale modeling based on both accuracy and

computational demands. Additionally, the anisotropic porosity model resolves flow variability at finer scales than isotropic models because the latter are constrained to scales larger than the REV.

Results show that significant differences may exist between pore-scale and point-scale flood conditions in close proximity to flow obstructions, for example due to wave reflections and wakes, so porosity model flood predictions should be used cautiously to inform point-scale flood risk decision-making, such as whether flood depths will rise above the threshold of a building door in a city. However, results validate the utility of porosity models for mapping pore-scale flood depths representative of average conditions across a roadway.

Further research into porosity models should be directed at reducing porosity model errors in velocity, for example with improved drag parameterizations, while remaining mindful of limitations posed by structural model errors. Finally, the cell averaging of fine-scale classical shallow-water model predictions is shown to enable a direct measure of porosity model error which is effective at gaging the merits of alternative porosity model formulations with respect to both flood depth and velocity prediction.

Acknowledgements

This work was supported by the MRPI program of the University of California Office of the President, the Infrastructure Management and Extreme Events program of the National Science Foundation (CMMI-1129730), and the Hazards-SEES program of the National Science Foundation (DMS-1331611). The authors wish to thank K. Yoon and his research team for their efforts to conduct the laboratory experiments presented here.

References

Arega, F., Sanders, B.F., 2004. Dispersion model for tidal wetlands. J. Hydraul. Eng. 130 (8), 739–754.
Bates, P.D., 2012. Integrating remote sensing data with flood inundation models: how far have we got? Hydrol. Process. 26, 2515–2521.
Bear, J., 1988. Dynamics of Fluids in Porous Media, Second ed. Dover Publ., New York (of the 1972 book) 761p.
Begnudelli, L., Sanders, B.F., Bradford, S.F., 2008. An adaptive Godunov-based model for flood simulation. J. Hydraul. Eng. 134 (6), 714–725.
Cea, L., Vázquez-Cendón, M.E., 2010. Unstructured finite volume discretization of two-dimensional depth-averaged shallow water equations with porosity. Int. J. Num. Meth. Fluid. 63, 903–930.
Chen, A., Evans, B., Djordjević, S., Savić, D.A., 2012. A coarse-grid approach to represent building blockage effects in 2D urban flood modelling. J. Hydrol. 426–427, 1–16.
Defina, A., 2000. Two-dimensional shallow flow equations for partially dry areas. Water Resour. Res. 36 (11), 3251–3264.
Guinot, V., 2012. Multiple porosity shallow water models for macroscopic modelling of urban floods. Adv. Water Resour. 37, 40–72.
Haaland, S.E., 1983. Simple and explicit formulas for the friction factor in turbulent pipe flow. J. Fluids Eng. 105 (1), 89–90.
Kim, B., Sanders, B.F., Schubert, J.E., Famiglietti, J.S., 2014. Mesh type tradeoffs in 2D hydrodynamic modeling of flooding with a Godunov-based flow solver. Adv. Water Resour. 68, 42–61.
McMillan, H.K., Brasington, J., 2007. Reduced complexity strategies for modelling urban floodplain inundation. Geomorphology 90, 226–243.
Munson, B.R., Young, D.F., Okiishi, T.H., 2006. Fundamentals of Fluid Mechanics, 5th ed. John Wiley & Sons, 769p.
Nepf, H.M., 1999. Drag, turbulence and diffusion in flow through emergent vegetation. Water Resour. Res. 35 (2), 479–489.
Sampson, C.C., Fewtrell, T.J., Duncan, A., Shaad, K., Horritt, M.S., Bates, P.D., 2012. Use of terrestrial laser scanning data to derive decimetric resolution urban inundation models. Adv. Water Resour. 41, 1–17.
Sanders, B.F., 2008. Integration of a shallow-water model with a local time step. J. Hydraul. Res. 46 (8), 466–475.
Sanders, B.F., Schubert, J.E., Gallegos, H.A., 2008. Integral formulation of shallow-water equations with anisotropic porosity for urban flood modeling. J. Hydrol. 362, 19–38.
Schubert, J.E., Sanders, B.F., 2012. Building treatments for urban flood inundation models and implications for predictive skill and modeling efficiency. Adv. Water Resour. 41, 49–64.
Soares-Frazão, S., Lhomme, J., Guinot, V., Zech, Y., 2008. Two-dimensional shallow-water model with porosity for urban flood modelling. J. Hydraul. Res. 46 (1), 45–64.
Soares-Frazão, S., Zech, Y., 2008. Dam-break flow through an idealized city. J. Hydraul. Res. 46 (5), 648–658.
Testa, G., Zuccala, D., Alcrudo, F., Mulet, J., Soares-Frazão, S., 2007. Flash flood flow experiment in a simplified urban district. J. Hydraul. Res. 45 (Extra Issue), 37–44.
Yoon, K., 2007. Experimental Study on Flood Inundation Considering Urban Characteristics (FFC06-05). Urban Flood Disaster Management Research Center, Seoul.
Yu, D., Lane, S.N., 2005. Urban fluvial flood modelling using a two dimensional diffusion-wave treatment, part 2: development of a sub-grid-scale treatment. Hydrol. Process. 20 (7), 1567–1583.